

## Supporting Information

# Revealing Microscopic Dynamics: In-situ Liquid-phase TEM for Live Observations of Soft Materials and Quantitative Analysis via Deep Learning

*Yangyang Sun<sup>1</sup>, Xingyu Zhang<sup>1,\*</sup>, Rui Huang<sup>2</sup>, Dahai Yang<sup>2</sup>, Juyeong Kim<sup>3</sup>, Junhao Chen<sup>2</sup>, Edison Huixiang Ang<sup>4</sup>, Mufan Li<sup>5</sup>, Lin Li<sup>6</sup>, Xiaohui Song<sup>2,\*</sup>,*

<sup>1</sup>Faculty of Materials and Manufacturing, Beijing University of Technology, Beijing 100124, China

<sup>2</sup>School of Materials Science and Engineering, Hefei University of Technology, Anhui Province, 230009, China

<sup>3</sup>Department of Chemistry and Research Institute of Natural Sciences, Gyeongsang National University, Jinju 52828, South Korea

<sup>4</sup>Natural Sciences and Science Education, National Institute of Education, Nanyang Technological University, Singapore 637616, Singapore

<sup>5</sup>Institute of Physical Chemistry, the College of Chemistry and Molecular Engineering, Pecking University, Beijing, 100871, China

<sup>6</sup>Beijing Shunce Technology Co., Ltd, Beijing, 102629, China

\* To whom correspondence may be addressed: [xiaohuisong@hfut.edu.cn](mailto:xiaohuisong@hfut.edu.cn); [xingyu0711@bjut.edu.cn](mailto:xingyu0711@bjut.edu.cn)

### Content:

Supplementary notes 1-3 (Experimental)

Supplementary discussion 1-3

Supporting Figures S1-15

Supporting movies 1-9

## Supplementary notes

### Supplementary note 1: graphene liquid cell (GLC) preparation

The GLC preparation was prepared following previous reported method with modification<sup>1,2</sup>.

(1) Cut out a roughly 2 cm<sup>2</sup> piece of premade graphene-on-copper which fits around 6 TEM grids.

NOTE: Using 3-layers graphene instead of single layer graphene encapsulates liquid pockets with higher success rates without losing resolution. Since graphene is an atomically thin, low-Z material, most resolution loss is from liquid thickness for graphene liquid cells.

(2) Clean the graphene using an acetone wash

Place the graphene-on-copper piece in a glass Petri dish and fill with acetone.

Gently heat the acetone solution (~50 °C) for 5 min, swirling the solution periodically.

Remove the graphene-on-copper piece from the acetone wash with tweezers and replace the acetone with new, clean acetone. Repeat the washing process a total of 3 times.

Let the graphene-on-copper air-dry thoroughly before going on to the next step.

(3) Lay down TEM grids on the graphene-on-copper piece

(4) Etch the copper using a sodium persulfate solution

(5) Wash the grids to clean off the sodium persulfate

### Supplementary note 2: in situ liquid phase TEM experiments

Normally, the sample loading procedure is as follows<sup>3,4</sup>: Take two graphene-coated TEM grids and place them graphene side up on a glass slide. Using a small surgical scalpel blade, cut off the edge of one of the graphene-coated TEM grids, approximately 1/4 of the area of the grid.

Prepare the solution to be encapsulated:

- (i) Place 0.4 μL droplet of solution to be encapsulated on the non-cut graphene-coated TEM grid center. Use a tweezer to hold the edge of the TEM grid down while placing the droplet so that the capillary forces do not pick up the TEM grid.
- (ii) Quickly and carefully place the graphene-coated TEM grid with the cut corner on top of the droplet; the goal is to have the second grid come to rest on top of the first grid with no liquid getting squeezed out.

- (iii) Wait 5 min to let graphene liquid cell pockets form: Some evaporation of the liquid may occur as the pockets are forming, but once a hermetic seal is formed, no additional liquid loss is likely.
- (iv) Place the graphene liquid cell in a traditional TEM single tilt holder, and Load the TEM holder into the TEM column. Then, use the nanoparticles and amorphous carbon in the sample to properly align the TEM beam, and image. Finally, remove the holder from the beam path and calibrate electron beam dose rate.
- (v) Beam calibration: Once the liquid sample is in place, measurements are taken to determine the electron beam's actual dose rate on the sample. This could involve current measurements, and then calculation based on the following equation:

$$\text{Dose Rate (Gy/s)} = \frac{\text{Beam Current (A)} \times \text{Electron Charge (C)}}{\text{Beam Area (cm}^2\text{)} \times \text{Electron Energy (eV)}}$$

**DI water:** The water solution utilized in this experiment is deionized water sourced from the Millipore Milli-Q® Integral 10 Water Purification System. The water employed is ultra-pure water, with a resistivity of 18.4 MΩ<sup>cm</sup>. The remaining experimental steps and details are the same as described above: approximately 0.4 μL of water droplet is deposited onto the graphene film, and then assembled into a liquid graphene pocket, serving as the sample for in situ liquid phase TEM experiments.

**Tween80 aqueous solution:** First, prepare a water solution of surfactant: The non-ionic surfactant Tween80 is used in this experiment, with a concentration of 5.0×10<sup>-7</sup> mol/L, and deionized water as the solvent. After preparing the solution, allow it to stand undisturbed to ensure uniformity and prevent the formation of any bubbles. Subsequently, the experimental steps and details are the same as described above: approximately 0.4 μL of water droplet is deposited onto the graphene film, and then assembled into a liquid graphene pocket, serving as the sample for in situ liquid phase TEM experiments.

**Au NP aqueous solution:** Sodium citrate-stabilized gold nanoparticles, with a size of 15 nanometers, are dispersed in deionized water solution at a concentration of 0.005 mg/ml. This solution is utilized for in situ liquid-phase TEM experiments. The remaining steps are the same as previously described.

**Au NP in Tween80 aqueous solution:** Sodium citrate-stabilized gold nanoparticles, with a size of 15 nanometers, are dispersed in a Tween80 water solution with a concentration of  $5.0 \times 10^{-7}$  mol/L. The final concentration of gold nanoparticles in the solution is 0.005 mg/ml. After preparing the solution, allow it to stand undisturbed to ensure uniformity and prevent the formation of any bubbles. Subsequently, the in-situ imaging experimental steps and details are the same as described above.

**PS-b-PAA vesicle aqueous solution:** The preparation of vesicles following previous method<sup>5, 6</sup> with some modification: To synthesize PS<sub>144</sub>-b-PAA<sub>22</sub> vesicles, the following components were sequentially mixed in a vial: 410  $\mu$ L of DMF, 40  $\mu$ L of PS<sub>144</sub>-b-PAA<sub>22</sub> in DMF (4 mg/mL), 125  $\mu$ L of H<sub>2</sub>O, and 5  $\mu$ L of aqueous HCl solution (0.1 M). The resulting solution contains PS<sub>144</sub>-b-PAA<sub>22</sub> (0.28 mg/mL), HCl (0.91 mM), DMF (450  $\mu$ L), H<sub>2</sub>O (130  $\mu$ L), and has a  $V_{\text{DMF}}/V_{\text{w}}$  ratio of 45/13. The capped vial was incubated at 70°C in a temperature-controlled oil bath for 1 hour to facilitate the formation of vesicular micelles. Subsequently, the in-situ imaging experimental steps and details are the same as described above.

**S nanoparticle:** 200 nm S nanoparticles were dispersed in ethanol solution (0.01 mg/ml) and then dropped on GLC for encapsulation (after drying). Subsequently, the in-situ imaging experimental steps and details are the same as described above. Note: in this experiment, the graphene liquid cell only encapsulates the S nanoparticle, no liquid inside. This design is helpful to protect TEM inside environment (S evaporation could lead to some pollution).

**Au nanoplate:** CTAB-stabilized aqueous solution of 200-230 nm gold nanoplates was purchased from Beijing Zhongke Keyu Nanotechnology Co., Ltd. [CTAB] = 10 mM, 8 mg/mL. When in use, 0.5 ml of CTAB-stabilized 200-230 nm Au nanoplates is centrifuged, followed by rinsing once with DI water to remove excess CTAB in the solution, and finally dispersed in DI water for further use.

**Zeta potential of Au NPs:** The surface zeta potential of Sodium citrate-stabilized gold nanoparticles is -29 mV, and -25 mV in Tween80 solution. This negative zeta potential arises due to the adsorption of negatively charged citrate ions on the surface of the gold nanoparticles, leading to their stabilization, and imparting a negative charge to the particle surface in solution.

The surface zeta potential of CTAB-stabilized gold nanoparticles is 41 mV, and 37 mV in Tween80 solution. The positive zeta potential arises from the adsorption of the positively charged CTAB

molecules on the surface of the gold nanoparticles, resulting in a positive charge on the particle surface in solution.

### **Supplementary discussion 1 : image processing via deep learning (movies analysis)**

TEM (Transmission Electron Microscopy) movie processing analysis using Dragonfly deep learning involves employing advanced artificial intelligence techniques to extract valuable insights and information from dynamic sequences of TEM images, often referred to as "movies." Dragonfly, a deep learning framework, enhances the analysis of these movies by automating various tasks and

**Key Steps in TEM Movie Processing Analysis with Dragonfly Deep Learning:**

(1) Data Preparation:

The first step involves preparing the TEM movie data for analysis. This includes converting the movie frames into a suitable format, ensuring proper alignment, and potentially applying pre-processing steps such as noise reduction or contrast enhancement.

(2) Training Deep Learning Models:

Dragonfly deep learning involves training neural network models to recognize and classify specific features or objects of interest within the TEM movie frames. This training process requires annotated data where these features are manually labeled. For example, if the goal is to track nanoparticles or structural changes in the movie, the neural network is trained to identify and locate them accurately.

(3) Feature Extraction:

Once trained, the deep learning model can automatically extract features or objects from each frame of the TEM movie. This could include identifying nanoparticles, defects, or other structural elements that are critical for the analysis.

(4) Object Tracking:

Dragonfly can track identified features across consecutive frames, allowing the visualization and quantification of their movement, interactions, or changes over time. This is particularly useful for studying dynamic processes such as phase transformations or particle diffusion.

(5) Segmentation and Masking:

The deep learning model can segment specific regions of interest within the TEM movie frames. This enables more precise analysis by focusing on specific areas or objects, reducing noise and improving accuracy.

(6) Quantitative Analysis:

Dragonfly can perform quantitative measurements on the extracted features, such as particle size distribution, velocity, intensity changes, and more. These measurements provide valuable insights into the underlying phenomena being studied.

(7) Visualization and Interpretation:

The processed and analyzed TEM movie data can be visualized using various tools and techniques. This includes generating heatmaps, trajectory plots, or overlaying tracking information onto the original movie frames. These visualizations aid in understanding the dynamics and behaviors of the observed materials or processes.

(8) Validation and Iteration:

The results obtained from the deep learning analysis can be validated against ground truth or known results, and the model can be refined iteratively for improved accuracy and robustness.

Overall, TEM movie processing analysis using Dragonfly deep learning enables researchers to gain a deeper understanding of dynamic processes, characterize materials at a finer level, and uncover hidden insights that might be challenging or time-consuming to achieve through manual analysis. This approach accelerates research, enhances data interpretation, and paves the way for new discoveries in the field of nanomaterials and materials science.

### **Supplementary discussion 2 : bubble dynamics via in-situ TEM imaging**

Drawing upon the insights gleaned from related literature<sup>7-9</sup>, the observed phenomenon of beam-induced bubble formation in both water and surfactant solutions reveals intriguing differences in their dynamics. Literature across diverse fields of interfacial science underscores the significance of surfactants in modulating bubble behavior, influencing stability, and interfacial tension<sup>10-12</sup>. This aligns with established knowledge wherein surfactants play a pivotal role in altering the properties of liquid interfaces, impacting phenomena like Ostwald ripening, interfacial tension reduction, and stability enhancement.

Moreover, previous studies examining the impact of external stimuli, akin to the electron beam's influence, on liquid systems have highlighted transformative effects on nanomaterials' self-

assembly or structural alterations<sup>4, 13, 14</sup>. However, the specific role of surfactants within these contexts is less explored.

This study's potential significance lies in elucidating the nuanced influence of surfactants on beam-induced bubble dynamics, a facet that necessitates rigorous control experiments to disentangle the surfactant's contribution from other influential factors. The synthesis of our findings with existing literature underscores the novelty and importance of comprehensively understanding the interplay between surfactants, external stimuli, and bubble dynamics, potentially opening avenues for tailored material design and interfacial manipulation.

### **Supplementary discussion 3 : electron beam effects**

The study of nano bubbles using in situ liquid phase transmission electron microscopy (TEM) provides valuable insights into their behavior and properties under controlled conditions. When considering the electron beam effect on nano bubbles, two key factors come into play: electron-beam-induced radiolysis and heating effects<sup>11, 15-17</sup>. These factors can have varying implications when comparing the behavior of nano bubbles in deionized (DI) water and surface aqueous solutions.

#### **(1) Electron-Beam-Induced Radiolysis:**

In both DI water and surface aqueous solutions, the electron beam can induce radiolysis, leading to the generation of free radicals and other reactive species. These species can influence the stability and dynamics of nano bubbles. For instance, in DI water, the radiolysis products might have a higher impact due to the absence of stabilizing agents or solutes. This could potentially lead to more significant bubble growth or collapse events compared to surface aqueous solutions where stabilizing molecules might attenuate the radiolysis effects.

#### **(2) Heating Effects:**

Electron beam interactions with the liquid sample result in localized heating, causing thermal effects. In DI water, which has relatively lower thermal conductivity, the electron beam-induced heating can lead to rapid temperature increases around the nano bubbles. This could potentially cause bubble expansion or even boiling. In contrast, surface aqueous solutions containing stabilizing

agents may better disperse and dissipate the heat generated by the electron beam, resulting in more controlled temperature variations around the nano bubbles.

(3) Stability and Dynamics:

Nano bubbles in DI water might experience more drastic changes in stability and dynamics due to the potentially higher influence of radiolysis products and rapid heating effects. In surface aqueous solutions, the presence of stabilizing agents could dampen the impact of radiolysis and provide more stable conditions for the bubbles.

(4) Life time:

The combination of radiolysis and heating effects could potentially lead to shorter bubble lifetimes in DI water due to more intense and rapid changes. Surface aqueous solutions might exhibit longer-lasting bubbles due to the mitigating influence of stabilizing agents.

## Supporting Figures S1-S14

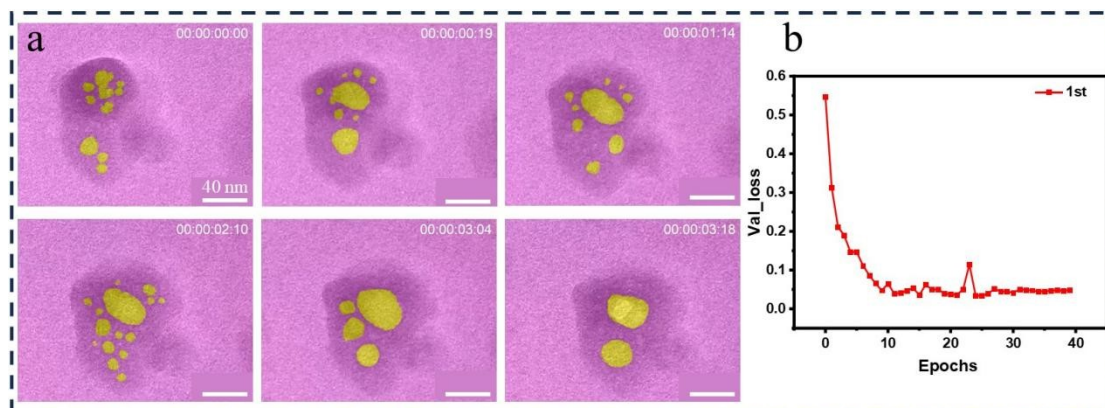


**Fig. S1 a:** Changes in the images of bubbles in the solution under electron beam irradiation and loss function **b.**

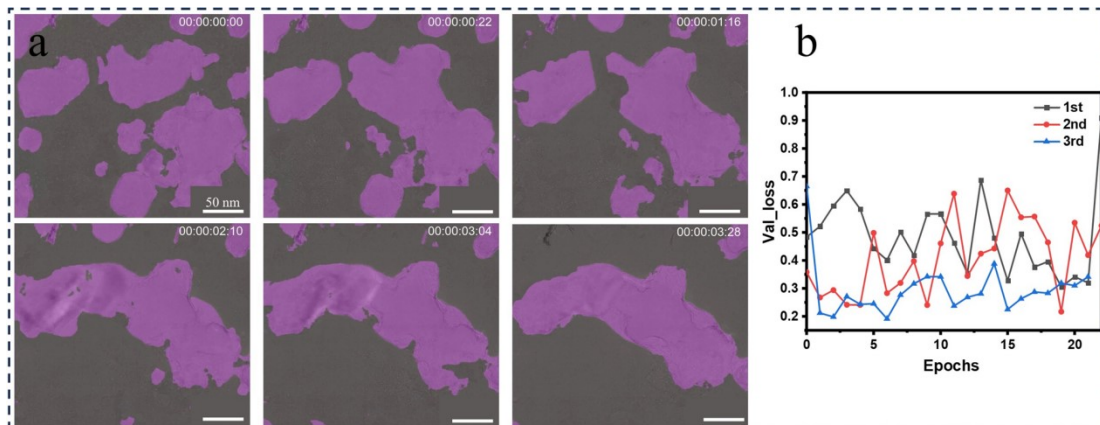


**Fig. S2 a:** Images depicting the evolution of bubble morphology over time upon the addition of surfactant, and loss function curve **b**

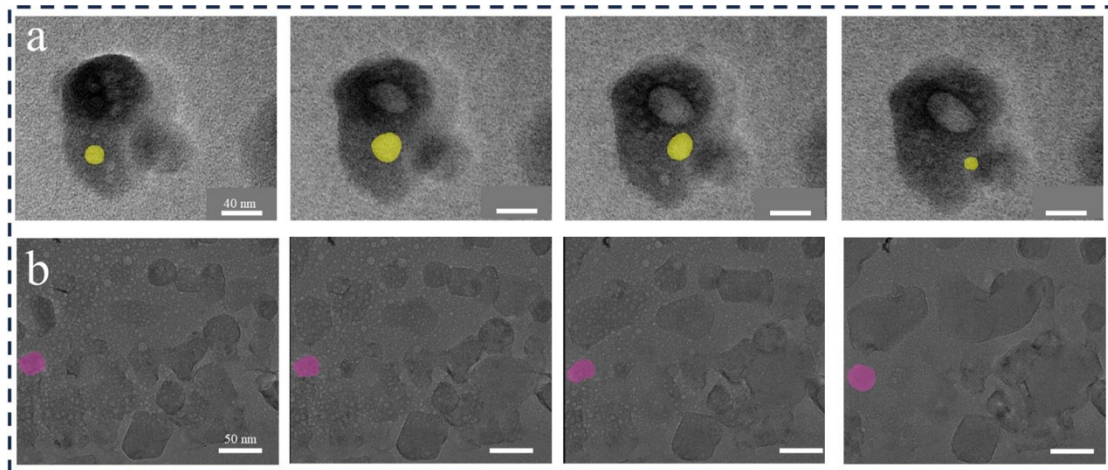


**Fig. S3 a** Morphological changes and motion trajectory of a bubble in deionized water; **b:** Images depicting the morphological changes and displacement over time of a bubble in a surfactant solution.

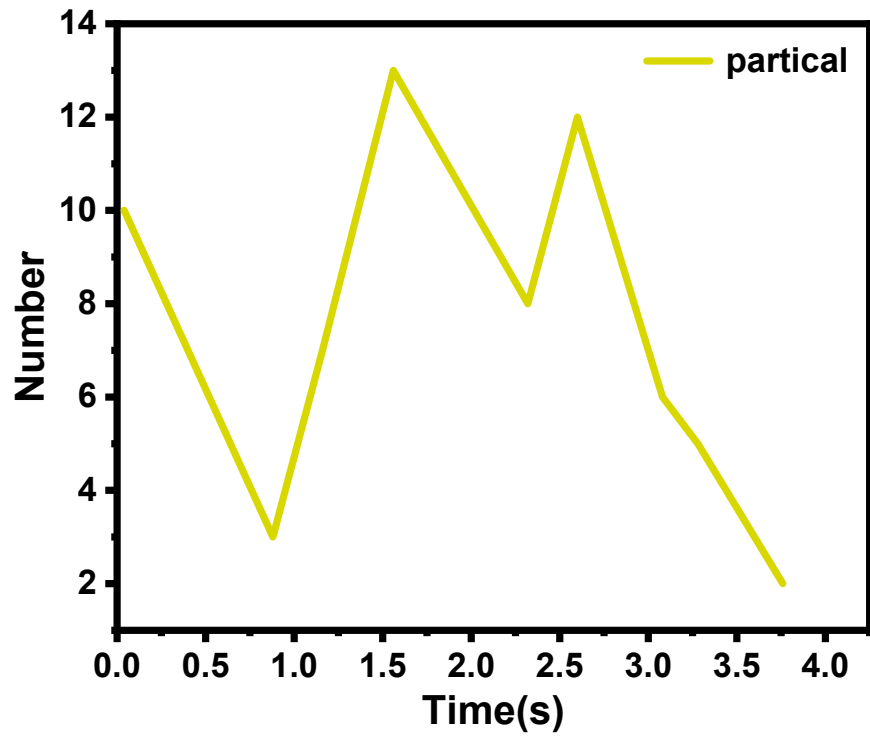


**Fig. S4** The number of bubbles change under in situ liquid phase TEM, due to the merge of the bubbles in DI water.

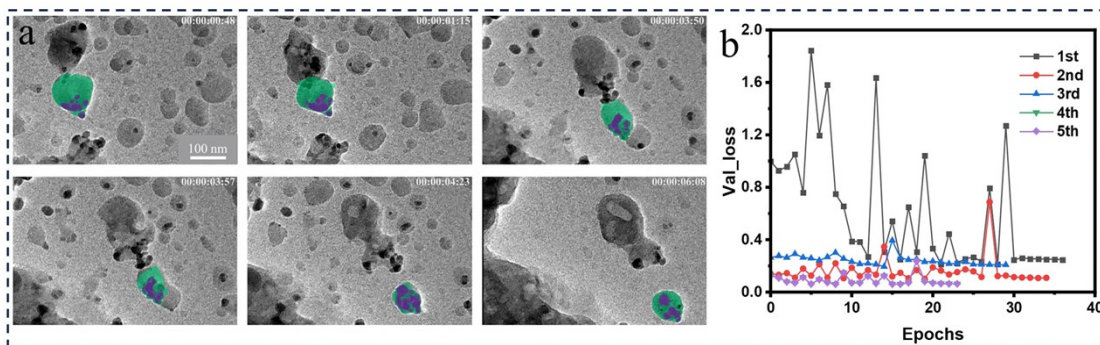


**Fig. S5 a:** Changes in the morphology and position of nanoparticles in deionized water solution with respect to time, along with the loss function; **b:** Images depicting the morphological changes and displacement of nanoparticles within bubbles over time.

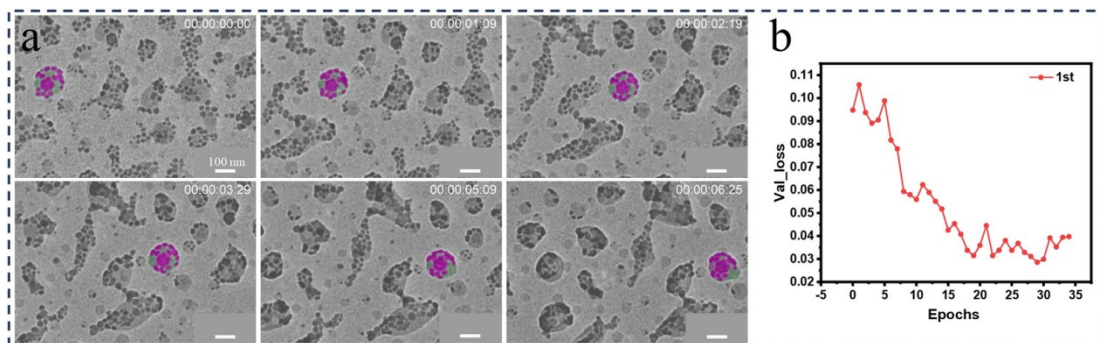


**Fig. S6 a:** Changes over time in the morphology of 15-nanometer gold nanoparticles within bubbles in a Tween 80 water solution, along with the loss function; **b:** Images depicting the evolution of bubble and gold nanoparticle morphology over time.

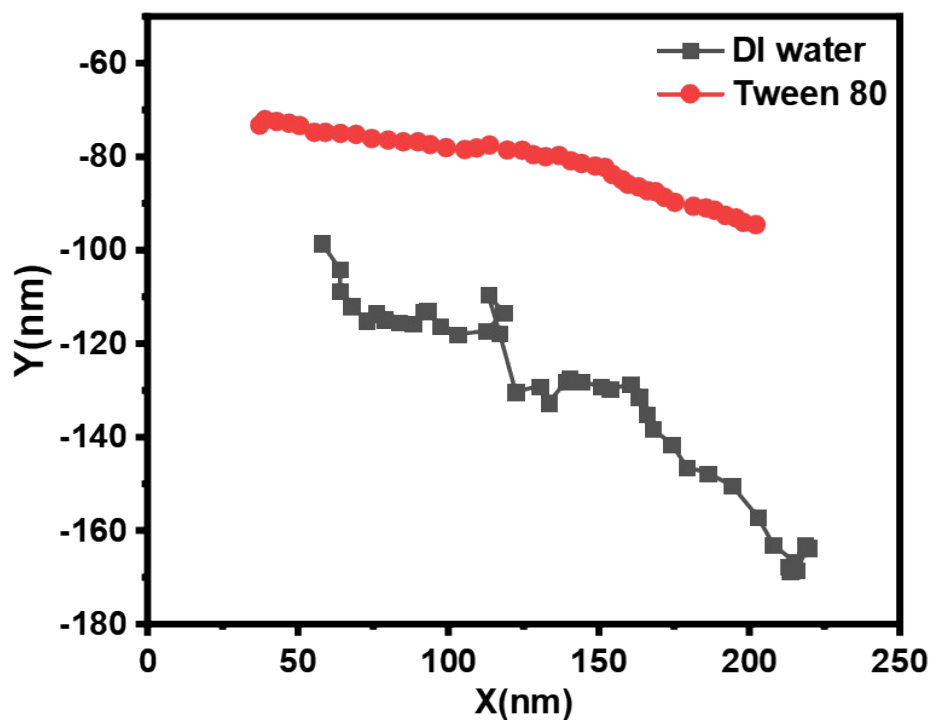


**Fig. S7** Movement trajectory plots of the two types of bubbles mentioned above in deionized water and Tween 80 water solution at the same time. (X and Y represent the position coordinates of nanoscale bubbles within the observation plane, indicating the movement of the bubble within the field of view)

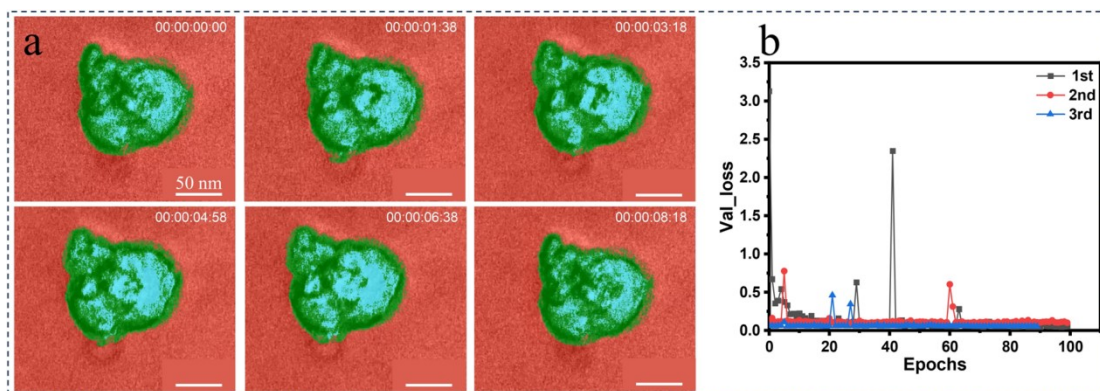


**Fig. S8 a** : TEM images depicting the temporal evolution of the 'self-cleaning' process within the assembly of PS-PAA vesicle structures (identified and labeled), and the loss function curve processed through deep learning; **b**: Loss function curve.

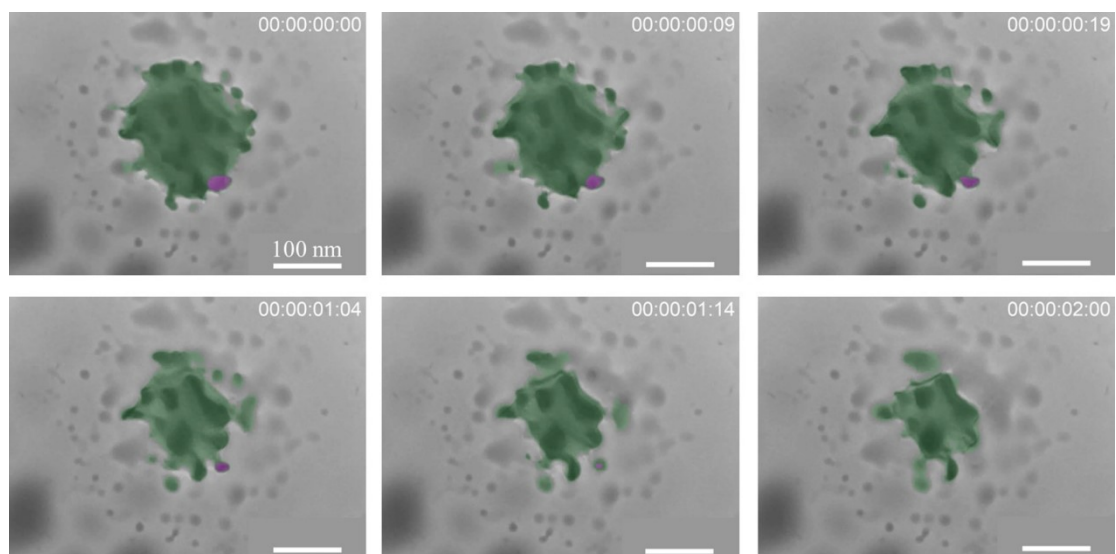


**Fig. S9** In-situ liquid-phase TEM of nanoscale sulfur particles during drying by evaporation: Under the influence of an electron beam, nanoscale sulfur transitions from a solid state to a liquid state and undergoes evaporative drying. The green region represents the overall liquid sulfur, while the purple indicates the independent drying process of mini liquid droplets.

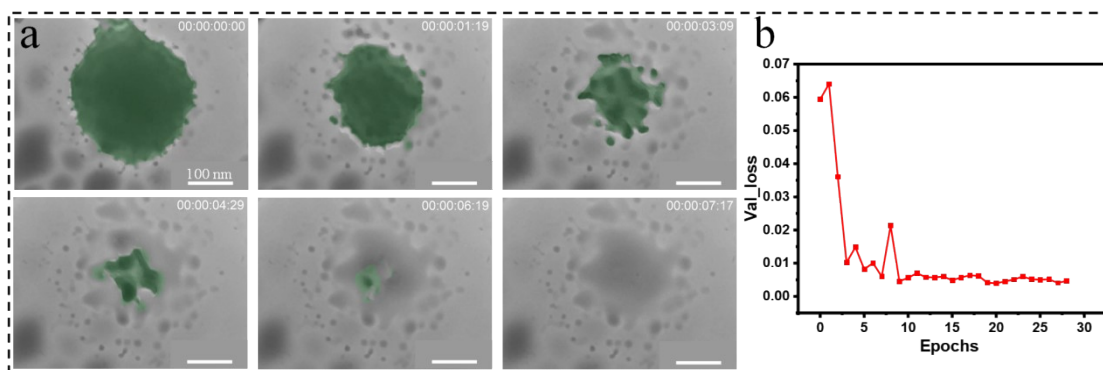


**Fig. S10 a:** Evaporation process of nanoscale sulfur observed under in-situ liquid-phase TEM, and the loss function curve processed through deep learning; **b:** Loss function curve.

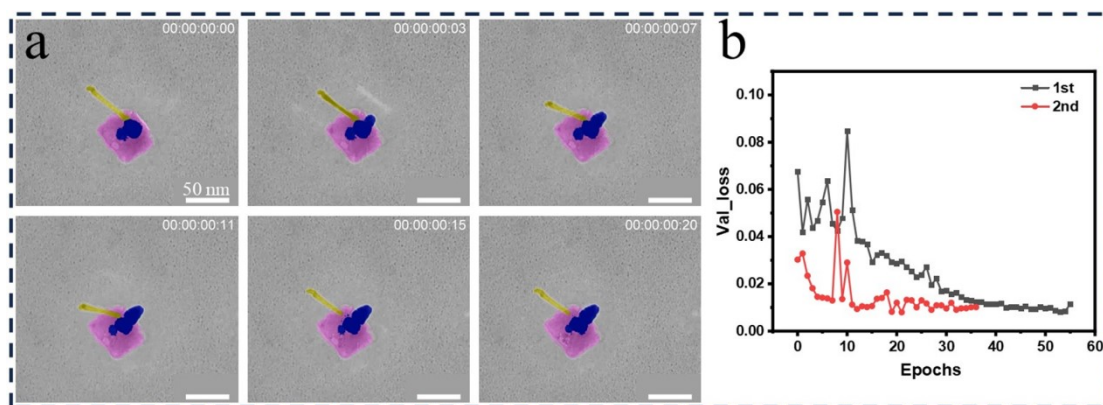


**Fig. S11 a:** Growth process (highlighted in yellow) of gold nanowires in a water solution with PVP as a ligand and surfactant, and ascorbic acid as a reducing agent, and **b:** the loss function curve processed through deep learning.

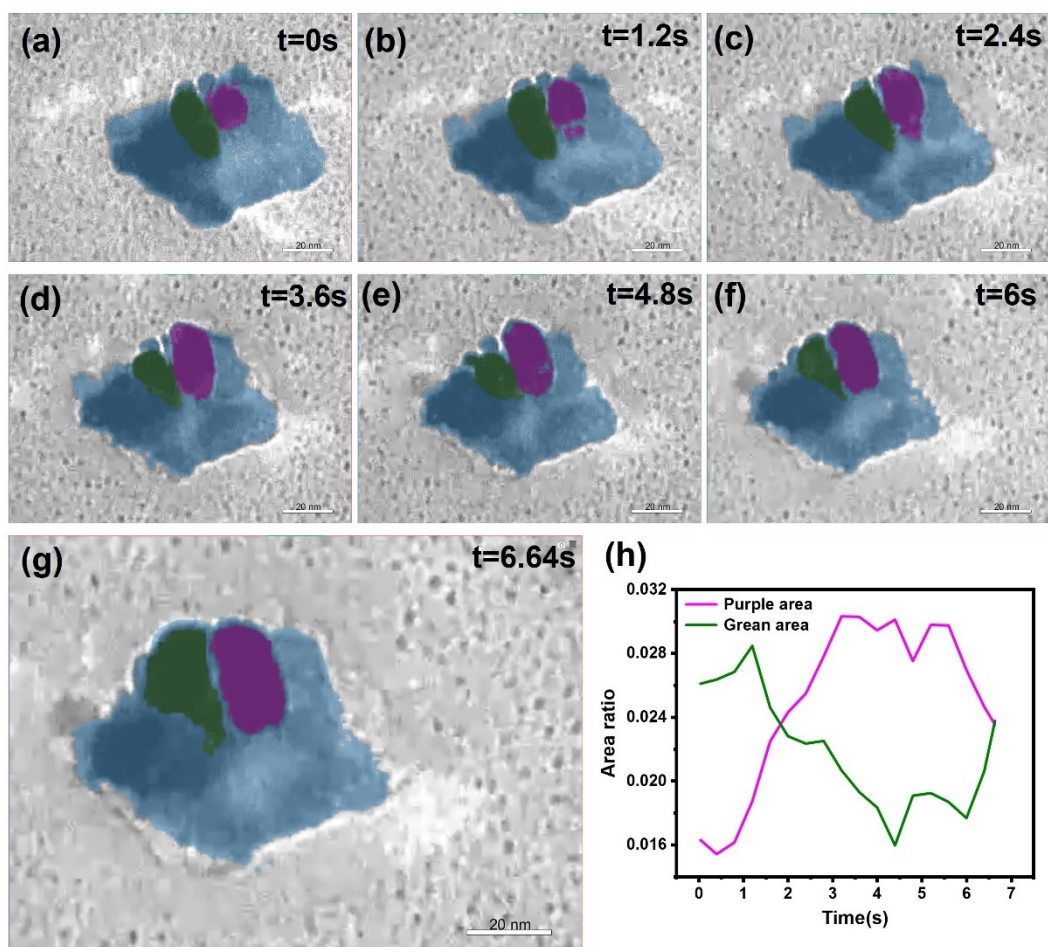


**Fig. S12 (a-g):** Growth process (highlighted in yellow) of gold crystal in a water solution without PVP presence, and ascorbic acid as a reducing agent, and **(h):** the area value change during the Ostwald ripening process between the two Au nanocrystals. Notably, in Figure h, the smooth curve represents the curve fitted via Moving Average according to the original data, used to depict the trend of changes over time.

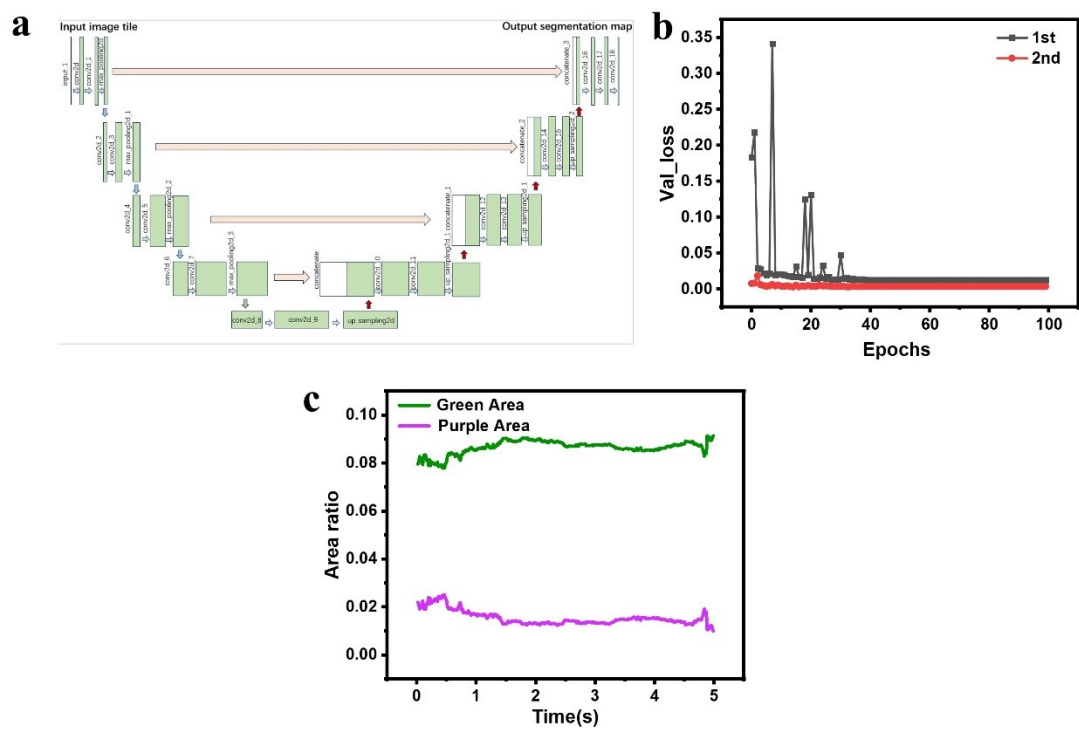


**Fig.S13** Utilizing deep learning to process the Au nucleation dynamics on CTAB stabilized Au nanoplate: **a**: 5-layer U-Net training model, **b**: the loss function curve processed through deep learning, **c**: area-time curve of Au nanoplate (green) and Au NPs (purple).

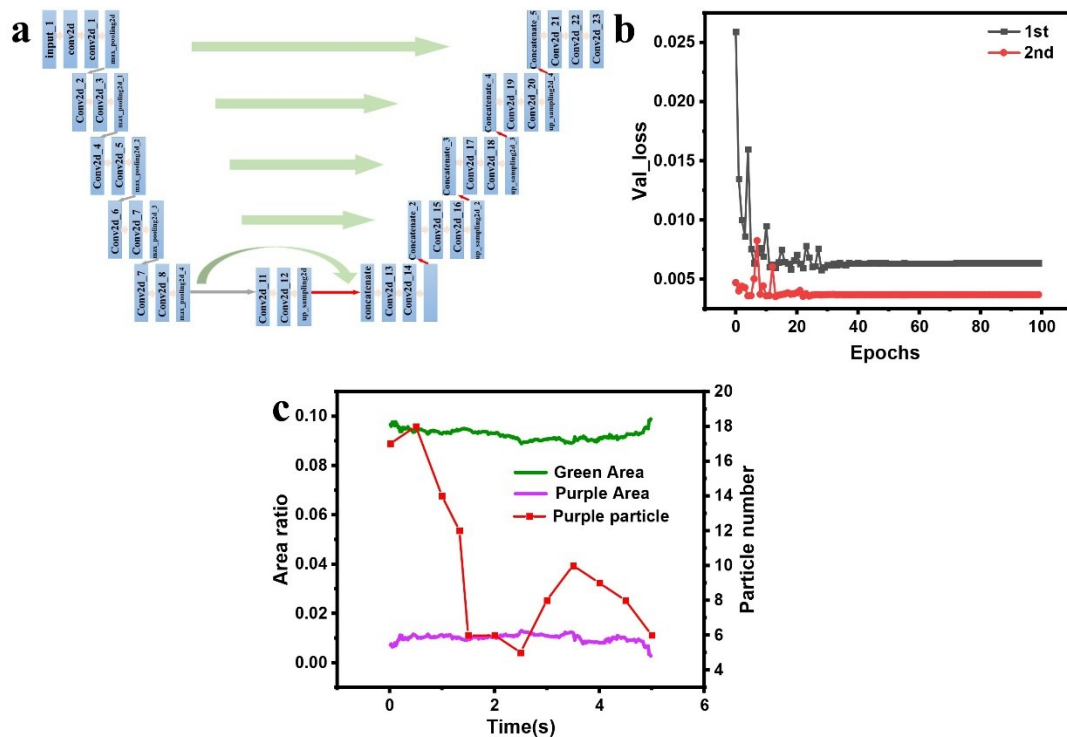


**Fig.S14** Utilizing deep learning to process the Au nucleation dynamics on CTAB stabilized Au nanoplate: **a**: 6-layer U-Net training model, **b**: the loss function curve processed through deep learning, **c**: area-time curve of Au nanoplate (green) and Au NPs (purple), and the number changes of Au nanoparticles during the deposition (red). Notably, In Figure c, the smooth curve represents the curve fitted via Moving Average according to the original data, used to depict the trend of changes over time.

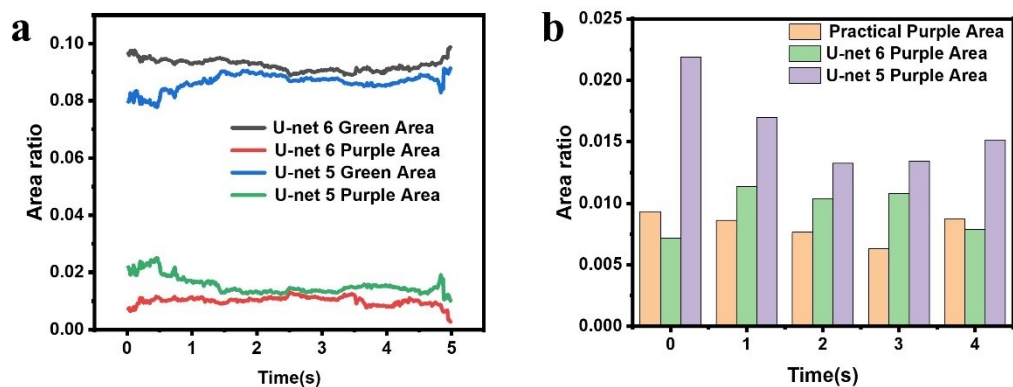


**Fig.S15** The comparison of 5-layer and 6-layer U-Net data processing: **a**: area-time curve of Au plate and Au nanoparticle, **b**: the bar chart of area ratio-time for different calculation methods including manual tracking, 5-layer and 6-layer U-Net deep learning training.

### **Supporting movies**

#### **Supporting movie 1:** bubbles in DI water under in-situ liquid phase TEM

Imaging condition: The in situ liquid-phase TEM studies were conducted in a 120 kV TEM-1400 Flash TEM (JEOL Ltd., Tokyo, Japan) equipped with a Gatan camera (Gatan Inc., Pleasanton, CA, USA). The in-situ image series were acquired at a rate of 2 frames per second and an incident electron flux of  $<0.1 \text{ e}^- \text{ \AA}^{-2} \text{ s}^{-1}$ .

Movie play speed: x 10 times of real speed

#### **Supporting movie 2:** bubbles in Tween80 aqueous solution under in-situ liquid phase TEM

Imaging condition: The in situ liquid-phase TEM studies were conducted in a 120 kV TEM-1400 Flash TEM (JEOL Ltd., Tokyo, Japan) equipped with a Gatan camera (Gatan Inc., Pleasanton, CA, USA). The in-situ image series were acquired at a rate of 2 frames per second and an incident electron flux of  $<0.1 \text{ e}^- \text{ \AA}^{-2} \text{ s}^{-1}$ .

Movie play speed: x 10 times of real speed

#### **Supporting movie 3:** Au NP aqueous solution under in-situ liquid phase TEM

Particle size: 13-15 nm

Imaging condition: The in situ liquid-phase TEM studies were conducted in a 120 kV TEM-1400 Flash TEM (JEOL Ltd., Tokyo, Japan) equipped with a Gatan camera (Gatan Inc., Pleasanton, CA, USA). The in-situ image series were acquired at a rate of 2 frames per second and an incident electron flux of  $<0.15 \text{ e}^- \text{ \AA}^{-2} \text{ s}^{-1}$ .

Movie play speed: x 6 times of real speed

#### **Supporting movie 4:** Au NP in Tween80 aqueous solution under in-situ liquid phase TEM

Particle size: 13-15 nm

Imaging condition: The in situ liquid-phase TEM studies were conducted in a 120 kV TEM-1400 Flash TEM (JEOL Ltd., Tokyo, Japan) equipped with a Gatan camera (Gatan Inc., Pleasanton, CA, USA). The in-situ image series were acquired at a rate of 2 frames per second and an incident electron flux of  $<0.15 \text{ e}^- \text{ \AA}^{-2} \text{ s}^{-1}$ .

Movie play speed: x 6 times of real speed

#### **Supporting movie 5:** PS-b-PAA vesicle in solution under in-situ liquid phase TEM

Imaging condition: The in situ liquid-phase TEM studies were conducted in a 120 kV TEM-1400 Flash TEM (JEOL Ltd., Tokyo, Japan) equipped with a Gatan camera (Gatan Inc., Pleasanton, CA, USA). The in-situ image series were acquired at a rate of 2 frames per second and an incident electron flux of  $<0.1 \text{ e}^- \text{ \AA}^{-2} \text{ s}^{-1}$ .

Movie play speed: x 5 times of real speed

#### **Supporting movie 6:** S nanoparticle under in-situ liquid phase TEM

Particle size: 100-150 nm

Imaging condition: The in situ liquid-phase TEM studies were conducted in a 100 kV TEM-1400 Flash TEM (JEOL Ltd., Tokyo, Japan) equipped with a Gatan camera (Gatan Inc., Pleasanton, CA, USA). The in-situ image series were acquired at a rate of 2 frames per second and an incident electron flux of  $<0.1 \text{ e}^- \text{ \AA}^{-2} \text{ s}^{-1}$ .

Movie play speed: x 5 times of real speed

**Supporting movie 7:** Au nanowire growth in PVP aqueous solution under in-situ liquid phase TEM

Imaging condition: The in situ liquid-phase TEM studies were conducted in a 120 kV TEM-1400 Flash TEM (JEOL Ltd., Tokyo, Japan) equipped with a Gatan camera (Gatan Inc., Pleasanton, CA, USA). The in-situ image series were acquired at a rate of 2 frames per second and an incident electron flux of  $<0.1 \text{ e}^- \text{ \AA}^{-2} \text{ s}^{-1}$ .

Movie play speed: x 10 times of real speed

**Supporting movie 8:** Au nanowire growth without PVP present in aqueous solution under in-situ liquid phase TEM, with beam ON/OFF as a control experiment.

Imaging condition: The in-situ liquid-phase TEM studies were conducted in a 120 kV TEM-1400 Flash TEM (JEOL Ltd., Tokyo, Japan) equipped with a Gatan camera (Gatan Inc., Pleasanton, CA, USA). The in-situ image series were acquired at a rate of 2 frames per second and an incident electron flux of  $<0.16 \text{ e}^- \text{ \AA}^{-2} \text{ s}^{-1}$ .

Movie play speed: x 10 times of real speed

**Supporting movie 9:** CTAB stabilized Au nanoplate in aqueous solution ([CTAB] = 5 mM) under in-situ liquid phase TEM at the presence of chloroauric acid (1 mM).

Imaging condition: The in situ liquid-phase TEM studies were conducted in a 120 kV TEM-1400 Flash TEM (JEOL Ltd., Tokyo, Japan) equipped with a Gatan camera (Gatan Inc., Pleasanton, CA, USA). The in-situ image series were acquired at a rate of 2 frames per second and an incident electron flux of  $<0.1 \text{ e}^- \text{ \AA}^{-2} \text{ s}^{-1}$ .

Movie play speed: x 5 times of real speed

## Supporting references

1. M. R. Hauwiller, J. C. Ondry and A. P. Alivisatos, *JoVE (Journal of Visualized Experiments)*, 2018, e57665.
2. M. R. Hauwiller, J. C. Ondry, C. M. Chan, P. Khandekar, J. Yu and A. P. Alivisatos, *Journal of the American Chemical Society*, 2019, **141**, 4428-4437.
3. Q. Chen, J. M. Yuk, M. R. Hauwiller, J. Park, K. S. Dae, J. S. Kim and A. P. Alivisatos, *MRS Bulletin*, 2020, **45**, 713-726.
4. D. Shin, J. B. Park, Y.-J. Kim, S. J. Kim, J. H. Kang, B. Lee, S.-P. Cho, B. H. Hong and K. S. Novoselov, *Nature communications*, 2015, **6**, 6068.
5. C. Liu, L. Yao, H. Wang, Z. R. Phua, X. Song and H. Chen, *Small*, 2014, **10**, 1332-1340.
6. S. Liu, C. Liu, X. Song, I. Kim and H. Chen, *RSC advances*, 2016, **6**, 98639-98645.
7. J. Yang, S. B. Alam, L. Yu, E. Chan and H. Zheng, *Micron*, 2019, **116**, 22-29.
8. T.-W. Huang, S.-Y. Liu, Y.-J. Chuang, H.-Y. Hsieh, C.-Y. Tsai, W.-J. Wu, C.-T. Tsai, U. Mirsaidov, P. Matsudaira and C.-S. Chang, *Soft Matter*, 2013, **9**, 8856-8861.
9. G. C. Egan, E. Y. Lau and E. Schwegler, *Nano Letters*, 2022, **22**, 1053-1058.
10. J. Liu, H. Huang, R. Liu, Z. Zhu, Q. Lei, A. Liu and Y. Li, *Journal of Nuclear Materials*, 2020, **537**, 152184.
11. Y. Bae, S. Kang, B. H. Kim, K. Lim, S. Jeon, S. Shim, W. C. Lee and J. Park, *Engineering*, 2021, **7**, 630-635.
12. S. B. Alam, J. Yang, K. C. Bustillo, C. Ophus, P. Ercius, H. Zheng and E. M. Chan, *Nanoscale*, 2020, **12**, 18606-18615.
13. Z. Zhang, J. Qiang, S. Wang, M. Xu, M. Gan, Z. Rao, T. Tian, S. Ke, Y. Zhou and Y. Hu, *Small*, 2021, **17**, 2103301.
14. T. Zhao, Y. Jiang, S. Luo, Y. Ying, Q. Zhang, S. Tang, L. Chen, J. Xia, P. Xue and J.-J. Zhang, *Lab on a Chip*, 2023, **23**, 3768-3777.
15. Q. Xiao, Y. Liu, Z. Guo, Z. Liu and X. Zhang, *Applied Physics Letters*, 2017, **111**.
16. B. H. Kim, J. Yang, D. Lee, B. K. Choi, T. Hyeon and J. Park, *Advanced Materials*, 2018, **30**, 1703316.
17. Y. Tomo, K. Takahashi, T. Nishiyama, T. Ikuta and Y. Takata, *International Journal of Heat and Mass Transfer*, 2017, **108**, 1460-1465.